Electrochimica Acta 174 (2015) 1122–1130

Contents lists available at ScienceDirect

Electrochimica Acta

journal homepage: www.elsevier.com/locate/electacta

Effects of fluorine doping on structure, surface chemistry, and electrochemical performance of $LiNi_{0.8}Co_{0.15}Al_{0.05}O_2$

Xiang Li[a,b], Zhengwei Xie[a,b], Wenjing Liu[a], Wujie Ge[a,b], Hao Wang[a,b], Meizhen Qu[a,*]

[a] Chengdu Institute of Organic Chemistry, Chinese Academy of Sciences, Chengdu 610041, PR China
[b] Graduate University of Chinese Academy of Sciences, Beijing 100039, PR China

ARTICLE INFO

Article history:
Received 30 April 2015
Received in revised form 18 June 2015
Accepted 22 June 2015
Available online 27 June 2015

Keywords:
LiNi0.8Co0.15Al0.05O2
Fluorine doping
Surface chemistry
Cycling performance
Stability

ABSTRACT

The performance of $LiNi_{0.8}Co_{0.15}Al_{0.05}O_2$ is shown to be improved by fluorine doping via a modified low-temperature method. Scanning electron microscopy shows that fluorine doping catalyzes the growth of the primary particles. X-ray diffraction (XRD) results reveal that all the synthesized materials have typical hexagonal structure without impurities. The lattice parameters calculated from the XRD data by Rietveld refinement methods indicate that the interslab spacing distance is enlarged by fluorine doping. Inductively coupled plasma atomic emission spectroscopy and energy-dispersive X-ray spectroscopy show that fluorine atoms are preferentially enriched on the surface of the particle. X-ray photoelectron spectroscopy indicates that the valence state of nickel ions at the surface is lowered. The cycling performance of modified samples at room temperature, at high temperature (55 °C), and at high upper cut-off potentials is improved. Electrochemical impedance spectroscopy measurements reveal that fluorine doping could lower the impedance rise during cycling and suppress the degradation of the cathode material.

1. Introduction

Lithium ion batteries are used worldwide as power sources in consumer electronics. $LiCoO_2$, the dominant cathode material, however, cannot meet the surging demand for large-scale applications of the high-energy battery packs used in electric vehicles and hybrid electric vehicles owing to its low energy density, high cost, and toxicity. Therefore, great efforts have been made to develop alternative cathode materials. $LiNi_{0.8}Co_{0.15}Al_{0.05}O_2$ (NCA) is a promising candidate owing to its high capacity, low cost, and environmental friendliness [1].

Although nickel substitution takes advantage of the synergistic effect of both enhancing the structural stability and maintaining high capacity, cathodes with a high nickel concentration suffer from a severe capacity fade inherited from $LiNiO_2$. The factors involved in the capacity fade of layered cathode materials can be categorized as follows.

- **Internal** Formation of stress-inducing microcracks at grain boundaries during long-term cycling by lattice expansion at high cut-off potentials [2], redox-irreversible second phases [3], and gradual increase in degree of cation mixing [4–6].
- **Interface interaction** Solid electrolyte interface film formation, rock salt NiO-like layer that propagates from the surface into the bulk of active materials [7], Li ion consumption by lithium carbonate formation [8–10], and HF attack and catalyst effect of transition metals at the surface of active materials [11].

Many investigations suggested that, among the factors mentioned above, the gradual formation of second phases contributes to most of the capacity fade. However, the capacity fade can be delayed in ways that lower the chemical reaction kinetics or the migration trend of transition metal ions under the same oxygen arrangement. Cation substitution (Mg^{2+} [12–14]) and surface modification (Ni_3PO_4 [15], AlF_3 [16], SiO_2 [17], TiO_2 [18], $LiCoO_2$ [19,20], $FePO_4$ [21], Li_2ZrO_3 [22], Li_2BO_3 [23]) are effective approaches to suppressing the phase transformation and side reactions at the interface, thus improving the structural stability and slowing the capacity fade to some extent.

Anion doping is considered an attractive strategy to improve the cycle stability and is adopted by many researchers to modify cathodes using anions such as F^- [24], Cl^- [25], Br^- [26], S^{2-} [27], and PO_4^{2-} [28]. Among these anions, fluorine doping was found to enhance the performance of the cathode materials $LiNi_{1-x-y}Co_xMn_yO_2$ [29–32], lithium-rich cathodes such as

---

[*] Corresponding author at: P.O. Box 415, Chengdu 610041, Sichuan Province, PR China. Tel.: +86 28 85228839; fax: +86 28 85215069.
E-mail addresses: bill90@126.com (X. Li), mzhqu@cioc.ac.cn (M. Qu).

http://dx.doi.org/10.1016/j.electacta.2015.06.099
0013-4686/

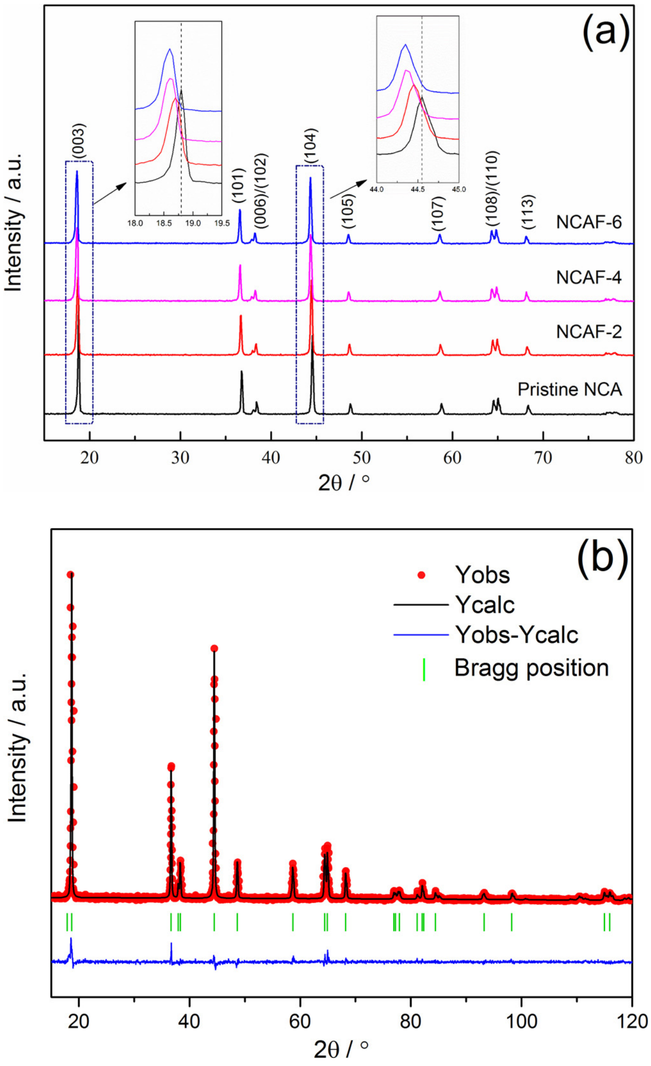

Fig. 1. XRD patterns of NCA and NCAFs (a) and Rietveld refinement results for NCAF-2 (b).

$Li_{1.05}(Ni_{0.5}Mn_{0.5})_{0.95}O_2$ [33], olive $LiFePO_4$ [34], and spinel $Li_4Mn_5O_{12}$ [35]. To date, the effect of anion doping on the stability of a high-nickel layered cathode of NCA has not been investigated.

Researchers recently presented a facile low-temperature calcination process to incorporate a significant amount of fluorine into the lattice of cathode materials [31,32,36–38]. This method is more advantageous than the common high-temperature calcination method. Here, a modified low-temperature method was adopted to modify the surface structure of NCA with NH_4F, and the effects of fluorine on the structure, surface chemistry, and electrochemical performances were investigated.

2. Experimental

2.1. Synthesis and characterization

The pristine precursor, $Ni_{0.8}Co_{0.15}Al_{0.05}(OH)_{2.05}$, with a spherical morphology was obtained by commercial supply. For a typical synthesis, the precursor and $LiOH{\cdot}H_2O$ with a molar ratio of 1:1.05 was mixed and ground thoroughly. After the mixed powder was sintered at 480 °C for 5 h under air and then at 750 °C for 15 h under oxygen flow, $LiNi_{0.8}Co_{0.15}Al_{0.05}O_2$ was obtained. Then, different amounts of NH_4F (2mol%, 4mol%, and 6mol%; the results are called NCAF-2, NCAF-4, and NCAF-6, respectively) were dissolved in 10 ml of alcohol, and the pristine NCA was also dispersed in a certain amount of alcohol. Next, the two solutions were blended under continuous magnetic stirring for 5 h. Finally, the slurry was dried and ground before calcination at 420 °C for 4 h under air, and the powder was quenched in air to obtain the final material.

The elemental concentrations of the NCA and NCAF samples were analyzed using inductively coupled plasma atomic emission spectroscopy (ICP-AES; IRIS 1000, Thermo Electron Corporation). Powder X-ray diffraction (XRD; X'Pert MPD DY1219) using Cu Kα radiation was employed to identify the crystalline phases of the synthesized materials. The lattice constants were calculated by the least square method. The microstructure and energy-dispersive X-ray spectroscopy (EDS) maps of the powders were observed by scanning electron microscopy (SEM; INCA Penta-FETx3). X-ray photoelectron spectroscopy (XPS; PHI5600 Physical Electronics) was performed to determine the relative amounts of fluorine and nickel ions in the electrodes.

2.2. Electrochemical measurement

The electrochemical properties were measured using a CR2032 coin-type half-cell, which contains a cathode and a Li metal anode separated by a porous polypropylene film (Celgard 2400). The cathode slurry was prepared by homogeneously mixing the active material, acetylene black, and a polyvinylidene difluoride binder in a mass ratio of 8:1:1 in *N*-methyl-2-pyrrolidone (NMP) solvent. Then the slurry was cast onto an aluminum foil. After drying for 12 h to eliminate the NMP solvent, the electrode laminate was punched into disks (10 mm in diameter) and dried in a vacuum oven at 105 °C overnight.

The coin cell was assembled entirely in an argon-filled glovebox. The electrolyte [Capchem Technology (Shenzhen) Co., Ltd.] consists of a solution of 1 mol dm^{-3} $LiPF_6$ in ethylene carbonate, dimethyl carbonate, diethyl carbonate (1:1:1, in volume). Note that all the pristine NCA for electrochemical tests was prepared using the same procedure as that for the NCAF to rule out the effects of ethanol and of annealing. Galvanostatic charge–discharge experiments were conducted on an automatic galvanostatic charge–discharge unit (Land CT 2001A, Wuhan, China) at C rates between 2.8 V and various charging cut-off potentials (4.1–4.5 V) vs Li^+/Li. Cyclic voltammetry (CV) and electrochemical

Table 1
Lattice parameters of pristine NCA and NCAFs obtained by Rietveld Refinement.

Sample	lattice parameters				$I_{(003)}/I_{(104)}$	Ni in Li site	Zox	Rwp%	S_{NiO_2} / (Å)[a]	I_{LiO_2} / (Å)[a]
	a /Å	c /Å	c/a /Å	V /Å^3						
NCA	2.8694(1)	14.2037(8)	4.9500	100.92	1.291	0.011(9)	0.2560(3)	11.4	2.197	2.538
NCAF-2	2.8705(1)	14.2089(6)	4.9501	101.41	1.283	0.017(5)	0.2568(3)	11.6	2.175	2.561
NCAF-4	2.8697(1)	14.2048(8)	4.9499	101.48	1.278	0.028(7)	0.2561(7)	11.9	2.194	2.541
NCAF-6	2.8702(1)	14.2044(9)	4.9489	101.51	1.218	0.038(6)	0.2571(3)	11.7	2.169	2.566

[a] Transition metal slab spacing (*S*) and lithium slab spacing (*I*) as defined in Ref [39].

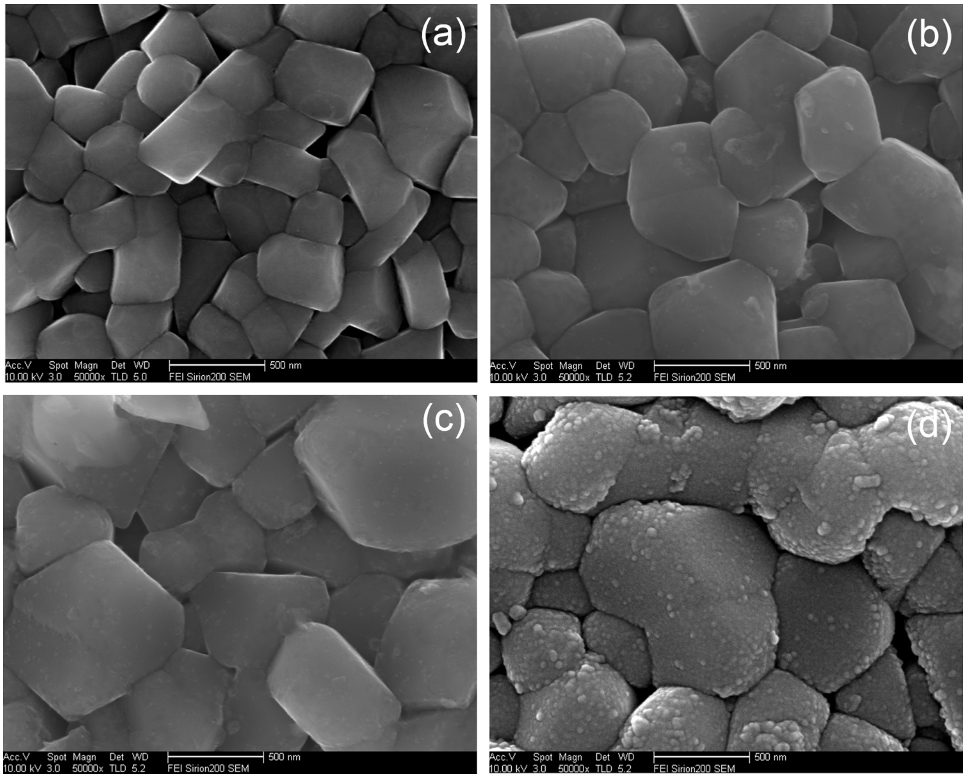

Fig. 2. SEM images of primary particles of pristine NCA (a) and NCAF-2 (b), NCAF-4 (c), NCAF-6 (d).

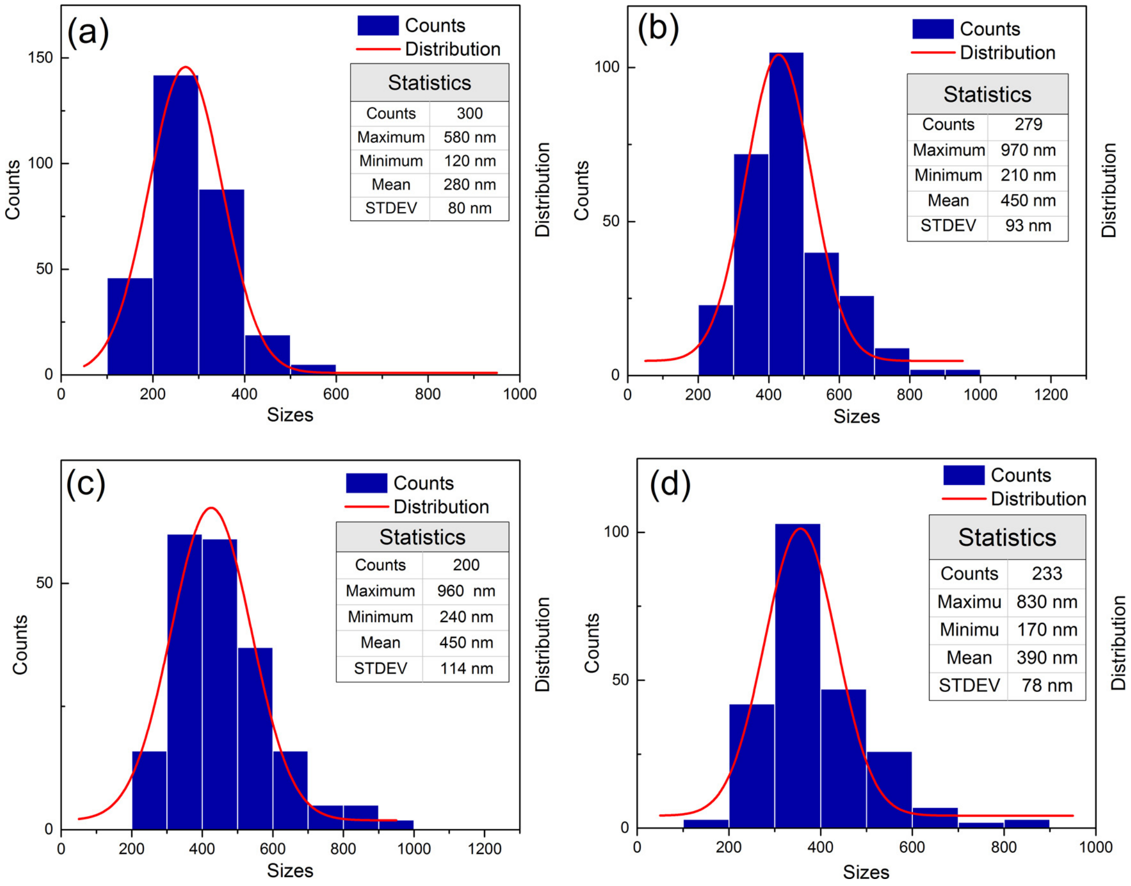

(a)

Statistics	
Counts	300
Maximum	580 nm
Minimum	120 nm
Mean	280 nm
STDEV	80 nm

(b)

Statistics	
Counts	279
Maximum	970 nm
Minimum	210 nm
Mean	450 nm
STDEV	93 nm

(c)

Statistics	
Counts	200
Maximum	960 nm
Minimum	240 nm
Mean	450 nm
STDEV	114 nm

(d)

Statistics	
Counts	233
Maximu	830 nm
Minimu	170 nm
Mean	390 nm
STDEV	78 nm

Fig. 3. Primary particle size (PPS) distribution estimated from more than 200 particles for each sample by SEM of pristine NCA(a), NCAF-2(b), NCAF-4(c), NCAF-6(d).

impedance spectroscopy (EIS) tests were conducted on a PARSTAT 2273 Electrochemical System (Princeton Applied Research, USA). For the CV measurements, the potential range was recorded from 2.8 to 4.5 V vs. Li^+/Li at 0.1 mV s^{-1}. The EIS measurements were performed over a frequency range from 10^5 Hz to 10^{-2} Hz with an input signal amplitude of 5 mV, and the measured data were fitted with Z-View software (Scribner Associates Inc.).

3. Results and discussion

Fig. 1 shows the XRD results. All the diffraction peaks can be indexed to a layered hexagonal structure of α-$NaFeO_2$ with space group $R\overline{3}m$. As presented in Fig. 1a, the modified materials exhibit no new peaks or impurities compared to the pristine NCA, which indicates that fluorine doping does not change the structure of

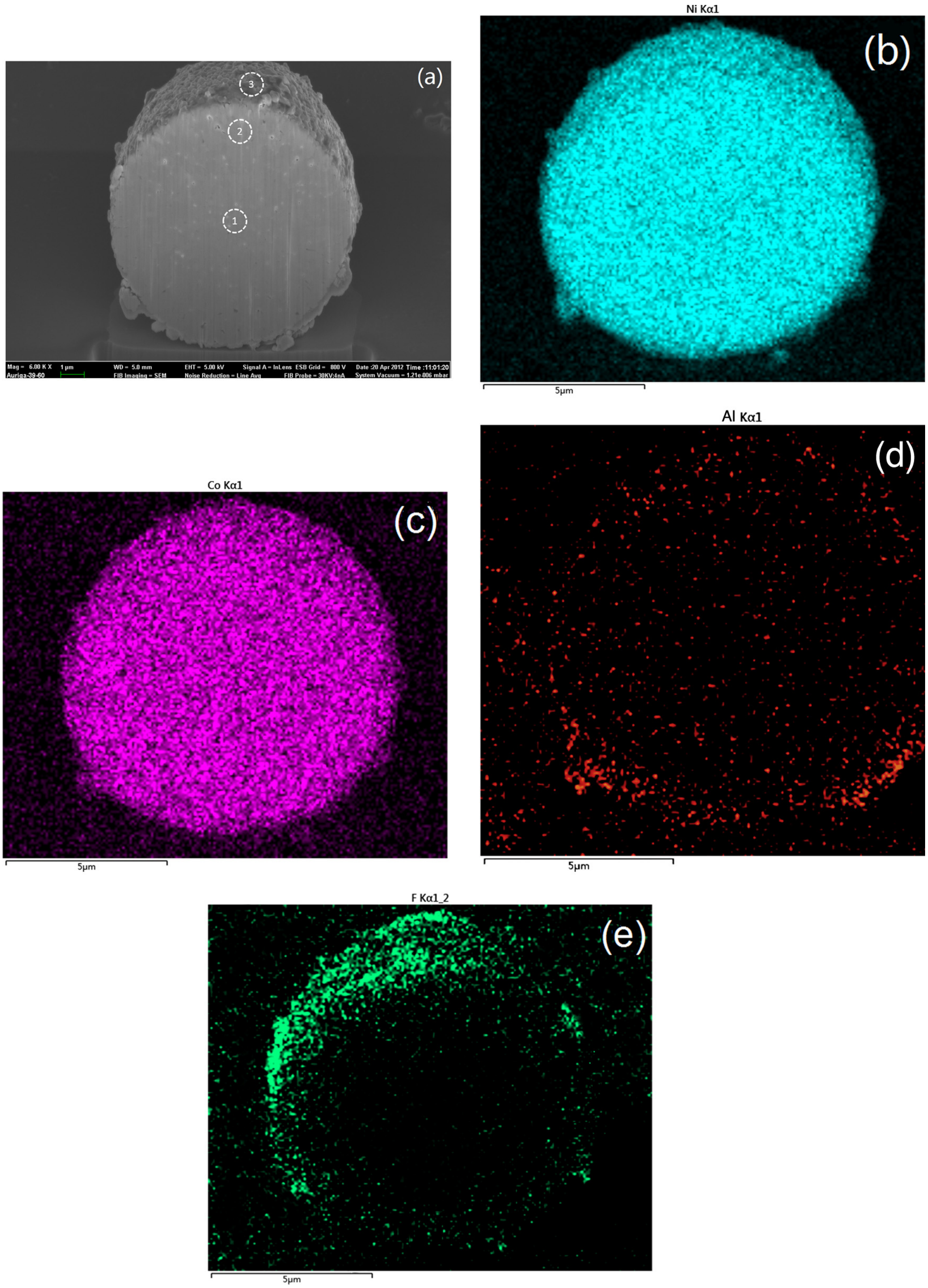

Fig. 4. EDS mappings of (b) Ni, (c) Co, (d) Al, (e) F for NCAF-2 particles (a).

Table 2
Results of the ICP analysis for NCA and NCAF-2.

Composition	Mole fraction of samples (±0.001)			
	Li	Ni	Co	Al
NCA	1.000	0.808	0.137	0.040
NCAF-2	1.017	0.817	0.138	0.041

Table 3
Surface elemental ratios obtained from EDS data.

Selected areas	Elemental mole ratio (±1)%			
	Ni	Co	Al	F
Area 1	81.1	14.9	3.8	0.2
Area 2	80.2	14.1	3.7	2.0
Area 3	73.0	13.1	4.0	9.9

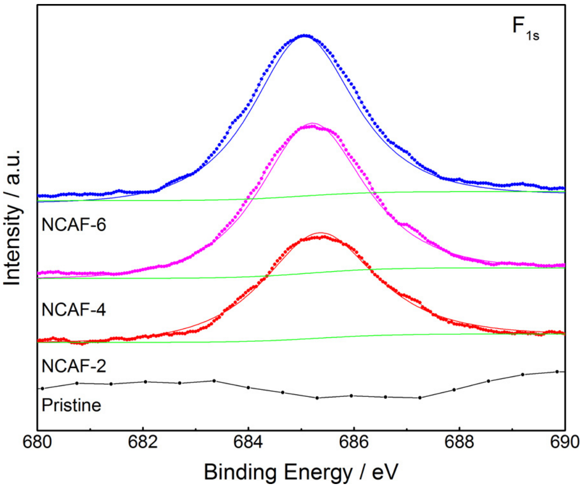

Fig. 5. XPS spectra of F_{1s} for pristine NCA and NCAFs.

NCA. The slightly shifted peaks shown in the inset of Fig. 1a imply that the crystal structure is slightly changed by fluorine doping, which is consistent with several reports [32,33].

The variations in the lattice parameters were calculated by Rietveld refinement. The results are presented in Table 1, and an example of full profile refinement for NCAF-2 is shown in Fig. 1b. We performed the refinements assuming a basic scenario: full and partial occupation of Ni in the Li layers. The reasonably small weighted profile R factor, R_{wp}, demonstrates that the proposed model is correct. The observed and calculated patterns match well, so the refinement is acceptable. It was found that with increasing fluorine concentration, the value of $I_{(003)}/I_{(104)}$ decreases, indicating an increased degree of cation mixing, which is consistent with the variations in the Ni occupancies at 3b sites. Further, the variation in the c axis is much larger than that in the a axis; this finding is related to the variation in the interslab distances, as listed in Table 1. Therefore, it is highly possible that the interslab distances might be enlarged after fluorine doping.

The morphology of the pristine sample and NCAF samples was examined by SEM (Fig. 2a–d). The pristine sample, NCAF-2 and NCAF-4 exhibited a smooth surface. Whereas, many small island-like particles were observed on the primary particles of NCAF-6, which form a strawberry-shaped sphere. Higher fluorine doping can have a larger effect on the morphology of the primary particles of NCA. The small particles on the surface may exist as an amorphous phase because the XRD results show no evidence of crystallization of any impurities.

As shown in Fig. 3, the primary particle size (PPS) distributions of the samples were measured randomly (more than 200 particles for each sample) by SEM, and the mean PPSs for NCA, NCAF-2, NCAF-4, and NCAF-6 are 280(±80) nm, 450(±93) nm, 450 (±114) nm, and 390(±78) nm, respectively. The mean PPS of the modified particles increased by more than 100 nm. It is reported that a small amount of ammonium fluoride may act as a mineralizing agent and can accelerate grain growth during high-temperature calcination [30,33]. The results presented here indicate that under low temperature, a small amount of fluorine doping can also help accelerate the growth of primary particles of NCA. These results suggest that fluorine doping alters the surface properties, growth kinetics, and final morphology of NCA [29].

Fig. 4 shows the EDS mappings of a cross-sectioned NCAF-2 sample. Fluorine atoms are detected on the cross-sectional surface, along with the other main components of the material. The main elements (Ni, Co, Al) in NCAF-2 are uniformly distributed, and their relative concentrations are not affected by fluorine doping, according to the ICP results presented in Table 2. However, the distribution of F atoms in the same area is quite selective, and it is focused on the surface of the particle. Further EDS measurements were conducted at the center, boundary, and outer surface of the particle in Fig. 4a, labeled points 1, 2, and 3 respectively. The molar ratios in these selected areas are listed in Table 3. The molar ratios of Co and Al approach stoichiometry in order from area 1 to 3. The Ni mole ratio varies greatly only in area 3. The F mole ratio gradually increases from 0.2% to 9.9% from area 1 to 3. This indicates that after this type of low-temperature calcination process, a large proportion of F atoms does not migrate into the deep center of spherical NCA particles. F may be preferentially enriched on the surface of the particles.

Fig. 5 shows the XPS analysis of the surfaces of pristine NCA and NCAF samples. The measured binding energy for F_{1s} is around 685 eV, which coincides with those of the metal fluorides NiF_2 and LiF, which lie between 650 and 685.9 eV [30,40]. This result indicates that the fluorine in the compound exists as F^-. As the amount of fluorine incorporated increases, the intensity of the F_{1s} peaks gradually increases. XPS analysis demonstrates that partial fluorine ion substitution successfully occurs at the oxygen sites; this is consistent with recent reports [31,32].

Fitted curves of Ni $2p_{3/2}$ for different samples are depicted in Fig. 6. The data on the relative content of nickel ions calculated from the plot are presented in Table 4. All the spectra were energy calibrated with the C 1s standard using the energy value of 284 eV. The spectra were then fitted using XPSPEAK software. The valences of Co and Al were both assumed to fix at +3. The ionic valence content could be estimated from the area under the curve, and the observed (black line) and calculated (dashed line) patterns match well, indicating that the results of fitting are accurate. As shown, the chemical state of Ni is changed by fluorine incorporation, and the concentration of Ni^{3+} is lowered. Considering that XPS is a type of surface analysis method, the variation in the Ni^{3+} concentration demonstrates that the surface contain less active Ni^{3+} after fluorine doping.

Fig. 7a illustrates the initial charge–discharge curves of NCA and NCAF cathodes at a constant current density of 0.1C (1C = 180 mAh g^{-1}) between 2.8 and 4.3 V vs. Li^+/Li at 25 °C. Clearly, the charge plateaus of the electrodes are raised gradually with increasing fluorine content in the initial charging, whereas the discharge curves of all the electrodes exhibit nearly the same value from 3.6 to 4.3 V. This phenomenon can be ascribed to the greater bonding strength of the Li–F bond than Li–O bond [41,42]. The pristine NCA delivers a discharge capacity of 198 mAh g^{-1}, and the NCAF electrodes show slightly lower capacities of 193 mAh g^{-1} for

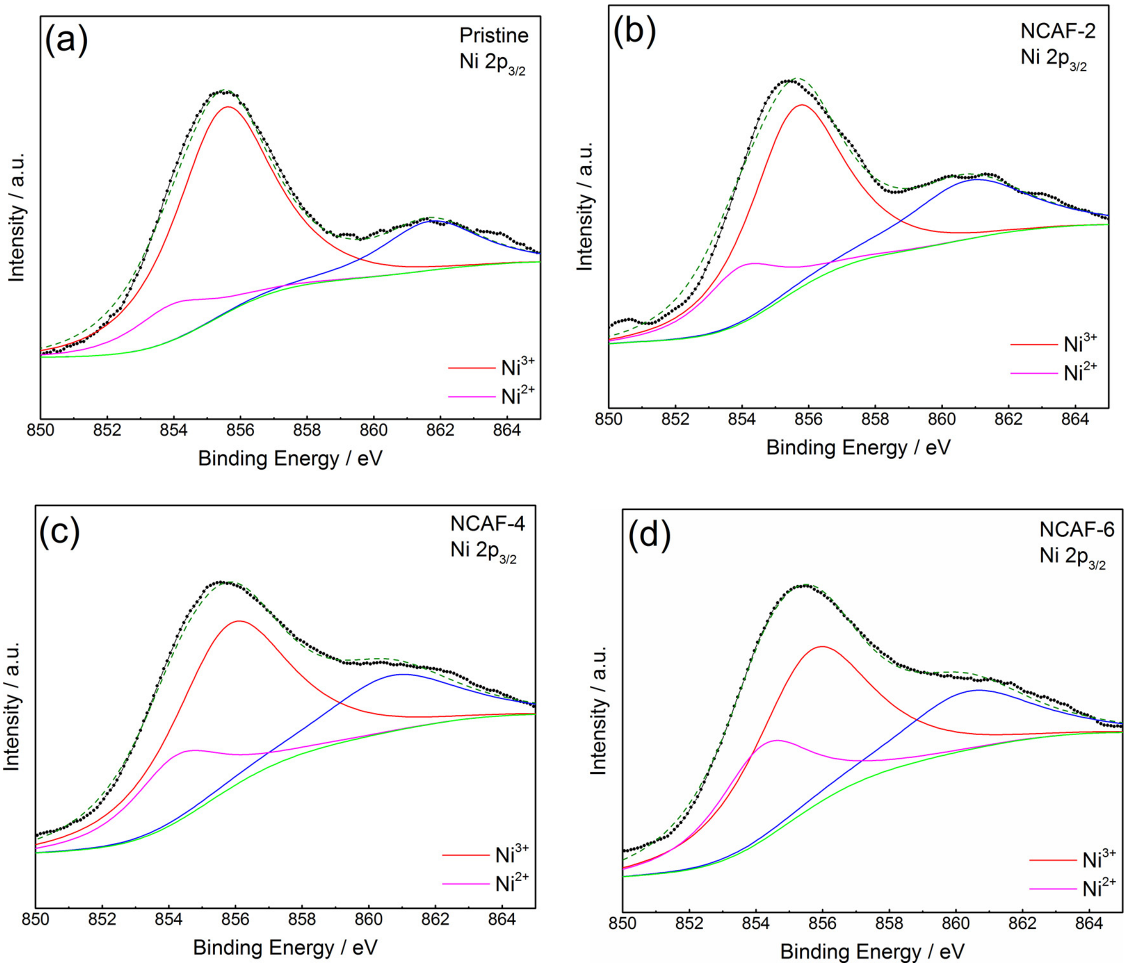

Fig. 6. XPS spectra and its corresponding fitting curves of Ni 2p for pristine NCA and NCAFs.

Table 4
Surface chemical states and mole fractions of nickel ions (Ni^{3+}) calculated from XPS fitting of pristine NCA and NCAFs.

Element	Pristine NCA	NCAF-2	NCAF-4	NCAF-6
Ni^{3+}%	86.99	79.17	75.70	66.95

NCAF-4 and 187.3 mAh g^{-1} for NCAF-6. Increasing the amount of fluorine induced partial reduction of nickel ions, which then tend to migrate to the lithium layer. This might result in the greater degree of cation mixing between Li^+ and Ni^{2+} [6], and thus the lower initial discharging capacity.

The cycling stability of the NCAF samples was tested under a constant current of 2C (Fig. 7b) at 25 °C. The pristine NCA show a large capacity fade after 100 cycles, whereas all of the NCAF samples exhibit enhanced cycling performance. The initial discharge capacity of the NCAF samples is lowered; however, the capacity retention rates are raised. NCAF-6 exhibits the best retention rate (97.1%), but it delivers a much lower discharging capacity (146 mAh g^{-1} at first cycle). NCAF-2 and NCAF-4 both show better cycling performance than the pristine sample. The NCAF-2 and the NCAF-4 deliver a discharging capacity of 161 mAh g^{-1} and 155 mAh g^{-1} (at first cycle) respectively, and has a retention rate of 94.1% and 94.8% respectively. While the pristine sample carries a discharging capacity of 167 mAh g^{-1} (at first cycle) and a retention rate of 85.6%.

Fig. 7c compares the discharge capacities of the electrodes at various C rates. All the samples show decreased capacities at high C rates, but those of the NCAF samples decrease slowly, exhibiting improved capacity retention rates over the C rate ranges. Although the discharge capacity of the pristine sample is higher than that of the NCAF samples at low C rates, it drops to 153 mAh g^{-1} at a rate of 5C, which is lower than that of NCAF-2 (158 mAh g^{-1}). Hence, an appropriate amount of fluorine doping is favorable for improving the rate capability of NCA.

The cycling performance of different samples at the same current of 2C at 55 °C is depicted in Fig. 7d. The pristine electrode delivers the highest discharge capacity, but the capacity retention is only 77.2% after 50 cycles. All the modified samples show enhanced capacity retention at 55 °C; NCAF-4 shows the best performance, and its retention rate (92.1%) is superior to that of the pristine sample.

To further test the overcharge properties, the NCAF-2 sample is chosen as an example to compare with the pristine sample. Both samples charged to higher upper cut-off potentials at 1C (Fig. 8). NCAF-2 clearly exhibits enhanced cycling performance with a high capacity retention, whereas the pristine NCA shows rapid capacity fading after 50 cycles, especially at 4.5 V. The capacity retention rates for pristine NCA and NCAF-2 are 77.8% and 86.8%, respectively, at an upper cut-off potential of 4.4 V vs. Li^+/Li. The values are 67.4% and 79.1%, respectively, at an upper cut-off potential of 4.5 V vs. Li^+/Li.

Fig. 9 shows the CV curves of NCA and NCAF-2 between 2.8 and 4.5 V vs. Li^+/Li at a scan rate of 0.1 mV s^{-1}. Both electrodes show three anodic peaks and three cathodic peaks. No significant change can be observed after fluorine doping after 2nd cycle. The CV curve

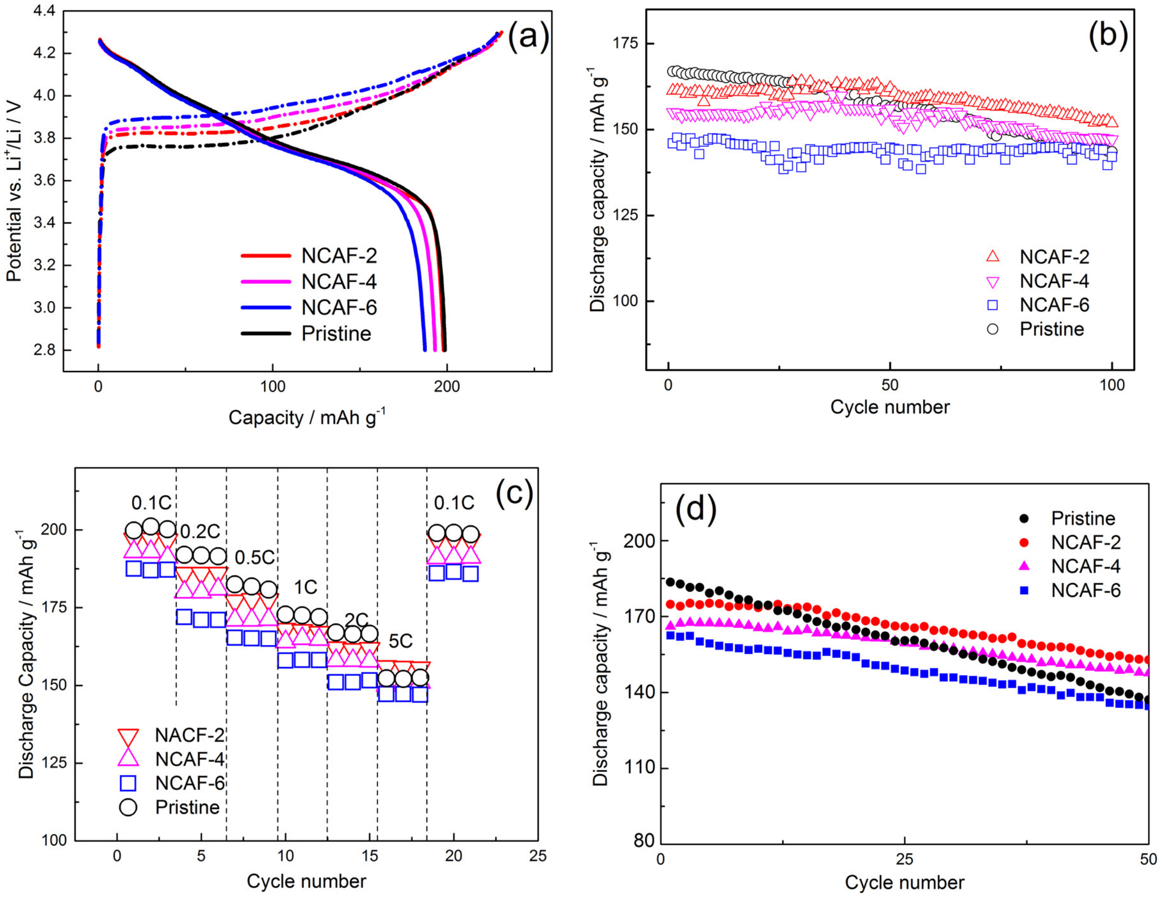

Fig. 7. (a) Initial discharge curves at a constant current of 18 mA g^{-1} at 25 °C; (b) cycling performance at a constant current of 360 mA g^{-1} at 25 °C; (c) C rates performance; (d) cycling performance at 55°C of NCA and NCAFs.

of the NCAF-2 sample is similar to that of the pristine sample, but the NCAF-2 sample exhibits a slightly higher potential than the pristine material. After 50th cycle, the pristine sample shows a larger polarization on the third redox peaks, while that is much smaller for the NCAF-2. This can be ascribed to the larger impedance rise of the pristine sample during cycling. Note that the area under the curve of the pristine is smaller than that of the NCAF-2, indicating larger capacity fade of the pristine sample, which is consistent with the cycling performance.

EIS measurement is a useful technique for studying the electrode kinetics of cathode materials. Fig. 10a, b show the Nyquist plots of pristine NCA and NCAF-2, respectively, after different cycles. As all of the electrodes were tested after different cycles in the charged state to 4.2 V vs. Li^+/Li, there appear two semicircles, which represent the surface film resistance and charge transfer resistance, respectively, and they are fitted using an equivalent circuit model with resistances R1 and R2 and constant

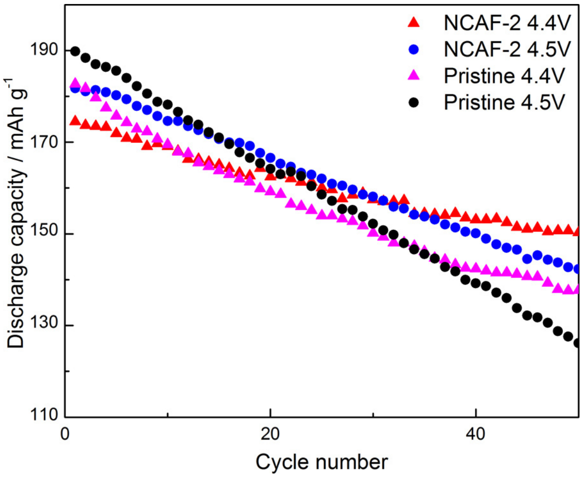

Fig. 8. cycling stability of pristine NCA and NCAF-2 at higher upper cut-off potentials (4.4 V, 4.5 V vs. Li^+/Li) at a constant current of 2C at 25 °C.

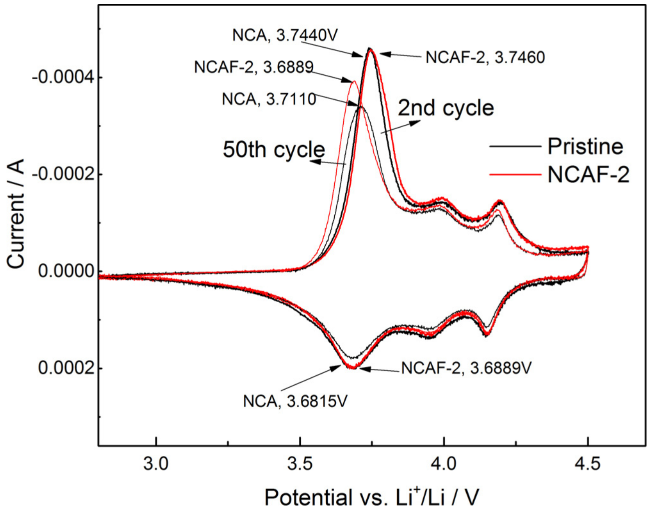

Fig. 9. Cyclic voltammograms of pristine NCA and NCAF-2 after 2nd and 50th cycle at a scan rate of 0.1 mV s^{-1} between 2.8 and 4.5 V vs. Li^+/Li at 25 °C.

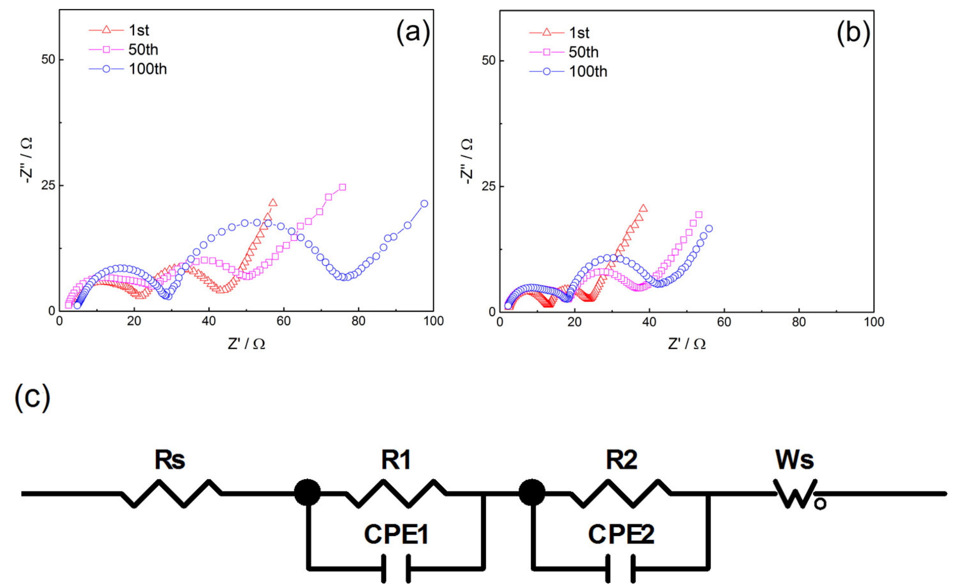

Fig. 10. EIS plots of electrodes after 1st, 50th, 100th cycles for pristine NCA (a) and NCAF-2 (b) at charged states; (c) equivalent circuit model used for fitting the EIS curves.

Table 5
Resistance values obtained from equivalent circuit fitting of experimental data for NCA and NCAF-2.

Parameters	R1+R2 / Ω		
Cycle	1st	50th	100th
NCA	22	28	39
NCAF-2	42	55	73

phase angle elements CPE1 and CPE2. As presented in Table 5, the values of R1+R2 for NCA and NCAF-2 increased after the 100th cycle. After the 1st cycle, R1+R2 is 42 and 22 Ω for NCA and NCAF-2, respectively. After the 100th cycle, the pristine NCA shows a much larger value of R1+R2 (73 Ω) than that of NCAF-2 (39 Ω), which is more relevant to the interior structure transformation. These results show that a small amount of fluorine doping can change the kinetics of cathode materials [43,44]. Although the degree of cation mixing is larger after fluorine doping, the nickel ions in the lithium layer somehow do not hinder the transportation of lithium ions. The larger interslab spacing distances might help improve Li ion transport at the surface, thus alleviating the impedance rise during cycling and lowering the capacity fade rate in the meantime.

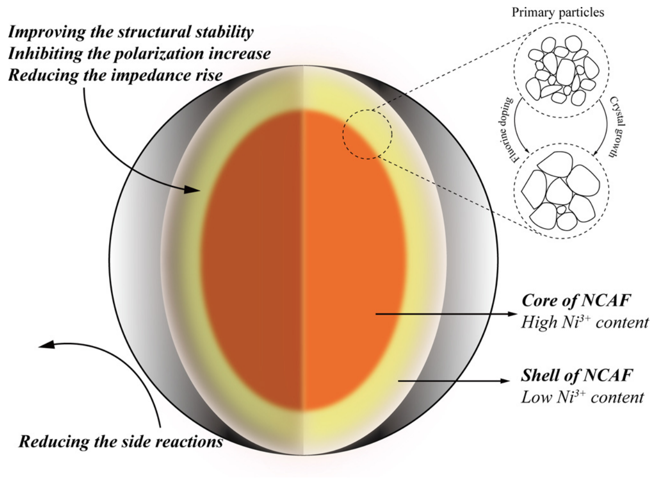

Fig. 11. Schematic of the effects of fluorine doping on NCA particle.

The effects of fluorine doping are illustrated in Fig. 11. During low-temperature calcination, fluorine ions might not infiltrate deeply into the cathode materials. They are incorporated into the surface layer of the cathode materials and might trigger the formation of a shell containing a lower concentration of active transition metal ions. This shell might serve to protect the core materials of NCA. The decrease in the active transition metal at the surface might reduce the side reactions at the interface and alleviate the decomposition of the electrolyte. The fluorine doping could help inhibit the polarization increase and reduce the impedance rise during cycling.

4. Conclusions

Fluorine-doped $LiNi_{0.8}Co_{0.15}Al_{0.05}O_2$ powders were successfully synthesized by a modified low-temperature method. SEM results showed that PPS of the NCAF samples was increased. XRD analysis found that all the NCAF electrodes had typical hexagonal structure without impurity phases. XPS analysis revealed that some fluorine ions were successfully substituted for oxygen in the lattice. The valence state of nickel ions at the surface was lowered. Although the initial discharge capacity was lowered, the cycling stability of the NCAF samples was enhanced, at high C rates, at high temperature, and at high upper cut-off potentials. CV and EIS further indicated that fluorine doping could help inhibit the polarization increase during cycling, decrease the impedance rise and improve the cycling performance.

Acknowledgments

This work was supported by the Major Program of the National Natural Science Foundation of China(Grant No. 51474196). We are also grateful for the help of the Analytical and Testing Center of Chengdu Branch, Chinese Academy of Sciences.

References

[1] C.H. Chen, J. Liu, M.E. Stoll, G. Henriksen, D.R. Vissers, K. Amine, Aluminum-doped lithium nickel cobalt oxide electrodes for high-power lithium-ion batteries, J. Power Sources 128 (2004) 278.

[2] S. Watanabe, M. Kinoshita, T. Hosokawa, K. Morigaki, K. Nakura, Capacity fade of $LiAl_yNi_{1-x-y}Co_xO_2$ cathode for lithium-ion batteries during accelerated calendar and cycle life tests (surface analysis of $LiAl_yNi_{1-x-y}Co_xO_2$ cathode after cycle tests in restricted depth of discharge ranges), J. Power Sources 258 (2014) 210.

[3] K. Kleiner, D. Dixon, P. Jakes, J. Melke, M. Yavuz, C. Roth, K. Nikolowski, V. Liebau, H. Ehrenberg, Fatigue of $LiNi_{0.8}Co_{0.15}Al_{0.05}O_2$ in commercial Li ion batteries, J. Power Sources 273 (2015) 70.

[4] S. Muto, Y. Sasano, K. Tatsumi, T. Sasaki, K. Horibuchi, Y. Takeuchi, Y. Ukyo, Capacity-fading mechanisms of $LiNiO_2$-based lithium-ion batteries II. Diagnostic analysis by electron microscopy and spectroscopy, J. Electrochem. Soc. 156 (2009) A371.

[5] T. Sasaki, T. Nonaka, H. Oka, C. Okuda, Y. Itou, Y. Kondo, Y. Takeuchi, Y. Ukyo, K. Tatsumi, S. Muto, Capacity-fading mechanisms of $LiNiO_2$-based lithium-ion batteries, J. Electrochem. Soc. 156 (2009) A289.

[6] E. Zhecheva, R. Stoyanova, R. Alcántara, P. Lavela, J.-L. Tirado, Cation order/disorder in lithium transition-metal oxides as insertion electrodes for lithium-ion batteries, Pure and Appl. Chem. 74 (2002) 1885.

[7] D.P. Abraham, R.D. Twesten, M. Balasubramanian, J. Kropf, D. Fischer, J. McBreen, I. Petrov, K. Amine, Microscopy and spectroscopy of lithium nickel oxide-based particles used in high power lithium-ion cells, J. Electrochem. Soc. 150 (2003) A1450.

[8] G.V. Zhuang, G.Y. Chen, J. Shim, X.Y. Song, P.N. Ross, T.J. Richardson, Li_2CO_3 in $LiNi_{0.8}Co_{0.15}Al_{0.05}O_2$ cathodes and its effects on capacity and power, J. Power Sources 134 (2004) 293.

[9] Y. Saito, M. Shikano, H. Kobayashi, State of charge (SOC) dependence of lithium carbonate on $LiNi_{0.8}Co_{0.15}Al_{0.05}O_2$ electrode for lithium-ion batteries, J. Power Sources 196 (2011) 6889.

[10] H. Visbal, S. Fujiki, Y. Aihara, T. Watanabe, Y. Park, S. Doo, The influence of the carbonate species on $LiNi_{0.8}Co_{0.15}Al_{0.05}O_2$ surfaces for all-solid-state lithium ion battery performance, J. Power Sources 269 (2014) 396.

[11] S.-U. Woo, C.S. Yoon, K. Amine, I. Belharouak, Y.-K. Sun, Significant improvement of electrochemical performance of AlF_3-coated $Li[Ni_{0.8}Co_{0.1}Mn_{0.1}]O_2$ cathode materials, J. Electrochem. Soc. 154 (2007) A1005.

[12] K. Tatsumi, Y. Sasano, S. Muto, T. Yoshida, T. Sasaki, K. Horibuchi, Y. Takeuchi, Y. Ukyo, Local atomic and electronic structures around Mg and Al dopants in $LiNiO_2$ electrodes studied by XANES and ELNES and first-principles calculations, Phys. Rev. B 78 (2008) 045108.

[13] S. Muto, K. Tatsumi, Y. Kojima, H. Oka, H. Kondo, K. Horibuchi, Y. Ukyo, Effect of Mg-doping on the degradation of $LiNiO_2$-based cathode materials by combined spectroscopic methods, J. Power Sources 205 (2012) 449.

[14] B. Huang, X.H. Li, Z.X. Wang, H.J. Guo, X.H. Xiong, Synthesis of Mg-doped $LiNi_{0.8}Co_{0.15}Al_{0.05}O_2$ oxide and its electrochemical behavior in high-voltage lithium-ion batteries, Ceram. Int. 40 (2014) 13223.

[15] D.-J. Lee, B. Scrosati, Y.K. Sun, $Ni_3(PO_4)$ 2-coated $LiNi_{0.8}Co_{0.15}Al_{0.05}O_2$ lithium battery electrode with improved cycling performance at 55 °C, J. Power Sources 196 (2011) 7742.

[16] S.-H. Lee, C.S. Yoon, K. Amine, Y.-K. Sun, Improvement of long-term cycling performance of $Li(Ni_{0.8}Co_{0.15}Al_{0.05})O_2$ by AlF_3 coating, J. Power Sources 234 (2013) 201.

[17] Y. Cho, J. Cho, Significant Improvement of $LiNi_{0.8}Co_{0.15}Al_{0.05}O_2$ Cathodes at 60°C by SiO_2 dry coating for Li-ion batteries, J. Electrochem. Soc. 157 (2010) A625.

[18] Y. Cho, Y.-S. Lee, S.-A. Park, Y. Lee, J. Cho, $LiNi_{0.8}Co_{0.15}Al_{0.05}O_2$ cathode materials prepared by TiO_2 nanoparticle coatings on $Ni_{0.8}Co_{0.15}Al_{0.05}(OH)_2$ Precursors, Electrochim. Acta 56 (2010) 333.

[19] W.M. Liu, G.R. Hu, K. Du, Z.D. Peng, Y.B. Cao, Surface coating of $LiNi_{0.8}Co_{0.15}Al_{0.05}O_2$ with $LiCoO_2$ by a molten salt method, Surf. Coat. Technol. 216 (2013) 267.

[20] W.M. Liu, G.R. Hu, K. Du, Z.D. Peng, Y.B. Cao, Enhanced storage property of $LiNi_{0.8}Co_{0.15}Al_{0.05}O_2$ coated with $LiCoO_2$, J. Power Sources 230 (2013) 201.

[21] B. Huang, X.H. Li, Z.X. Wang, H.J. Guo, A facile process for coating amorphous $FePO_4$ onto $LiNi_{0.8}Co_{0.15}Al_{0.05}O_2$ and the effects on its electrochemical properties, Mater. Lett. 131 (2014) 210.

[22] S. Ito, S. Fujiki, T. Yamada, Y. Aihara, Y. Park, T.Y. Kim, S.-W. Baek, J.-M. Lee, S. Doo, N. Machida, A rocking chair type all-solid-state lithium ion battery adopting Li_2O-ZrO_2 coated $LiNi_{0.8}Co_{0.15}Al_{0.05}O_2$ and a sulfide based electrolyte, J. Power Sources 248 (2014) 943.

[23] S.N. Lim, W. Ahn, S.-H. Yeon, S.B. Park, Enhanced elevated-temperature performance of $LiNi_{0.8}Co_{0.15}Al_{0.05}O_2$ electrodes coated with Li_2O-$2B_2O_3$ glass, Electrochim. Acta 136 (2014) 1.

[24] K. Kubo, M. Fujiwara, S. Yamada, S. Arai, M. Kanda, Synthesis and electrochemical properties for $LiNiO_2$ substituted by other elements, J. Power Sources 68 (1997) 553.

[25] X.L. Li, F.Y. Kang, W.C. Shen, X.D. Bai, Improvement of structural stability and electrochemical activity of a cathode material LiNi0. $7Co_{0.\ 3}O_2$ by chlorine doping, Electrochim. Acta 53 (2007) 1761.

[26] Y. Qi, Y. Huang, D. Jia, S.J. Bao, Z.P. Guo, Preparation and characterization of novel spinel $Li_4Ti_5O_{12-x}Br_x$ anode materials, Electrochim. Acta 54 (2009) 4772.

[27] Y.S. Sun, Jeon, Leeb, Overcoming jahn-teller distortion for spinel Mn phase, Electrochem. Solid-State Lett. 3 (2000) 7.

[28] H.Z. Zhang, Q.Q. Qiao, G.R. Li, X.P. Gao, PO_4^{3-} polyanion-doping for stabilizing Li-rich layered oxides as cathode materials for advanced lithium-ion batteries, J. Mater. A 2 (2014) 7454.

[29] G.H. Kim, J.H. Kim, S.T. Myung, C.S. Yoon, Y.K. Sun, Improvement of high-voltage cycling behavior of surface-modified $LiNi_{1/3}Co_{1/3}Mn_{1/3}O_2$ cathodes by fluorine substitution for Li-ion batteries, J. Electrochem. Soc. 152 (2005) A1707.

[30] S.-U. Woo, B.-C. Park, C.S. Yoon, S.-T. Myung, J. Prakash, Y.-K. Sun, Improvement of electrochemical performances of $LiNi_{0.8}Co_{0.1}Mn_{0.1}O_2$ cathode materials by fluorine substitution, J. Electrochem. Soc. 154 (2007) A649.

[31] P. Yue, Z.X. Wang, X.H. Li, X.H. Xiong, J.X. Wang, X.W. Wu, H.J. Guo, The enhanced electrochemical performance of $LiNi_{0.6}Co_{0.2}Mn_{0.2}O_2$ cathode materials by low temperature fluorine substitution, Electrochim. Acta 95 (2013) 112.

[32] P. Yue, Z.X. Wang, H.J. Guo, X.H. Xiong, X.H. Li, A low temperature fluorine substitution on the electrochemical performance of layered $LiNi_{0.8}Co_{0.1}Mn_{0.1}O_{2-z}F_z$ cathode materials, Electrochim. Acta 92 (2013) 1.

[33] H.L. Zhang, T.F. Song, Synthesis and performance of fluorine substituted $Li_{1.05}(Ni_{0.5}Mn_{0.5})_{0.95}O_{2-x}F_x$ cathode materials modified by surface coating with $FePO_4$, Electrochim. Acta 114 (2013) 116.

[34] X.Z. Liao, Y.S. He, Z.F. Ma, X.M. Zhang, L. Wang, Effects of fluorine-substitution on the electrochemical behavior of $LiFePO_4$/C cathode materials, J. Power Sources 174 (2007) 720.

[35] W. Choi, A. Manthiram, Influence of fluorine substitution on the electrochemical performance of 3V spinel $Li_4Mn_5O_{12-\eta}F_\eta$, Solid State Ionics 178 (2007) 1541.

[36] Q. Luo, A. Manthiram, Effect of low-temperature fluorine doping on the properties of spinel $LiMn_{2-2y}Li_yM_yO_{4-n}F_n$ (M = Fe, Co, and Zn) cathodes, J. Electrochem. Soc. 156 (2009) A84.

[37] W. Choi, A. Manthiram, Factors controlling the fluorine content and the electrochemical performance of spinel oxyfluoride cathodes, J. Electrochem. Soc. 154 (2007) A792.

[38] K.R. Stroukoff, A. Manthiram, Thermal stability of spinel $Li_{1.1}Mn_{1.9-y}MyO_{4-z}Fz$ (M = Ni, Al, and Li, $0 \leq y \leq 0.3$, and $0 \leq z \leq 0.2$) cathodes for lithium ion batteries, J. Mater. Chem. 21 (2011) 10165.

[39] M. Guilmard, C. Pouillerie, L. Croguennec, C. Delmas, Structural and electrochemical properties of $LiNi_{0.\ 70}Co_{0.\ 15}Al_{0.\ 15}O_2$, Solid State Ionics 160 (2003) 39.

[40] B.P. Löchel, H.H. Strehblow, Breakdown of passivity of nickel by fluoride, J. Electrochem. Soc. 131 (1984) 713.

[41] L. Liao, X.Y. Wang, X.F. Luo, X.M. Wang, S. Gamboa, P.J. Sebastian, Synthesis and electrochemical properties of layered $LiNi_{0.333}Co_{0.333}Mn_{0.293}Al_{0.04}O_{2-z}F_z$ cathode materials prepared by the sol-gel method, J. Power Sources 160 (2006) 657.

[42] Y.S. He, P. Li, X.Z. Liao, Z.F. Ma, Synthesis of $LiNi_{1/3}Co_{1/3}Mn_{1/3}O_{2-z}F_z$ cathode material from oxalate precursors for lithium ion battery, J. Fluorine Chem. 128 (2007) 139.

[43] O. Sha, Z. Tang, S. Wang, W. Yuan, Z. Qiao, Q. Xu, L. Ma, The multi-substitutedLi$Ni_{0.475}Al_{0.01}Cr_{0.04}Mn_{1.475}O_{3.95}F_{0.05}$ cathode material with excellent rate capability and cycle life, Electrochim. Acta 77 (2012) 250.

[44] C. Feng, H. Li, C. Zhang, Z. Guo, H. Wu, J. Tang, Synthesis and electrochemical properties of non-stoichiometric Li-Mn-spinel ($Li_{1.02}M_xMn_{1.95}O_{4-y}F_y$) for lithium ion battery application, Electrochim. Acta 61 (2012) 87.